Solar RRL

WILEY VCH

Solar RRL

RESEARCH ARTICLE OPEN ACCESS

Sequentially Evaporated Wide Bandgap Perovskite Absorber for Large-Area and Reproducible Fabrication of Solar Cells

Arman Mahboubi Soufiani | Hajar Moumine | Erik Wutke | Guillermo A. Farias Basulto | Wander Max Bernardes de Araujo | Matthew Leyden | Mateusz Szot | Tobias Bertram | Viktor Škorjanc | Angelika Harter | Stefanie Severin | Marcel Roß | Roland Mainz | Rutger Schlatmann | Steve Albrecht | Bernd Stannowski | Jona Kurpiers

Solar Energy Division, Helmholtz-Zentrum Berlin für Materialien und Energie GmbH, Berlin, Germany

Correspondence: Arman Mahboubi Soufiani (arman.mahboubi_soufiani@helmholtz-berlin.de) | Jona Kurpiers (jona.kurpiers@helmholtz-berlin.de)

Received: 30 May 2025 | **Revised:** 23 July 2025 | **Accepted:** 1 August 2025

Funding: Helmholtz-Association; European Union, Grant/Award Number: 101084251; Solar Technology Acceleration Platform; German Federal Ministry for Economic Affairs and Climate Action, Grant/Award Number: 03EE1041; KOALA-PLUS, Grant/Award Number: 03EE1109A; PeroQ2, Grant/Award Number: 03EE1183B; SHAPE, Grant/Award Number: 03EE1123 A-E; European Climate, Infrastructure and Environment Executive Agency

Keywords: perovskite solar cells | sequential evaporation | upscaling | wide bandgap

ABSTRACT

Herein, we perform sequential deposition of the organic and inorganic sub-components evaporated from *point sources*, followed by thermal conversion to yield wide bandgap perovskite films for the application in perovskite/silicon tandem cells. In our approach, uniform formamidinium iodide (FAI) layers with varying thicknesses are first deposited with rotating substrate. We next co-evaporate the inorganic precursors PbI_2, $PbBr_2$, and CsI onto the FAI layer in a static mode, without substrate rotation, leading to thickness gradients across the substrate, known from single-layer characterization. To promote conversion to α-phase perovskite, another uniform FAI layer is deposited on top, sandwiching the inorganic precursor layer stack. After thermal conversion, we obtain controlled compositional variations of the perovskite layer. Using spatially resolved characterization techniques, the most suitable composition, hence, evaporation rates for the individual inorganic precursors and the best thickness of the FAI sublayer are identified in a time-efficient manner. As a result, an optimized average implied open-circuit voltage, iV_{OC}, of about 1230 mV and optical bandgap of 1.70 eV, very uniformly distributed over a half M6 wafer area, were achieved for the absorbers when deposited on a self-assembled monolayer. Without any perovskite surface passivation or additional treatment, single-junction devices with an average fill factor of 70% (65%) in reverse (forward) light current–voltage scan and V_{OC} of 1075 mV were achieved across several batches. Integrating this absorber in tandem cells with a random-pyramid textured bottom-cell led to preliminary cells with efficiencies up to 24%.

1 | Introduction

The excitement around fabrication of high-efficiency monolithic perovskite/silicon tandem solar cells (PST) is now waning as more critical aspects of the technology must be addressed for it to become market relevant [1]. These include but are not limited to, scalability, reproducibility, and most importantly stability and reliability. The highest certified power conversion efficiency (PCE) of 34.85% reported so far for 2-terminal PSTs by the PV manufacturer LONGI [2, 3] is on laboratory-scale active area dimensions of approximately 1 cm^2. Yet, recent reports show success by industry in achieving performances higher than the record industrial single-junction (SJ) crystalline silicon (c-Si) solar cells of >27% on active areas larger than 200 cm^2 [2, 4].

While there is limited information published online by the so-far record-holding companies about their perovskite fabrication technique on large-area c-Si bottom-cells, it is speculated that these partly or fully involve a solution-based processing step. Among the relatively successful, scalable perovskite deposition techniques, published in the literature, are slot-die coating [5], physical vapor-phase deposition (PVD) such as sublimation through co- [6, 7] or sequential evaporation [8, 9], and hybrid processes [10, 11].

In commonly practiced solution-based processing methods, individual chemical components or precursors (e.g., organic and inorganic halide salts) are dissolved, in the right proportions, in the precursor solution enabling exact formation of the perovskite composition of interest when deposited onto an appropriate substrate and annealed under right conditions.

As opposed, in thermal evaporation-based methods, individual chemical components are generally sublimed or evaporated from separate sources (i.e., crucibles) ideally reaching the substrate surface in a timely manner, without reacting on the way to the substrate, to form the final composition during the deposition or upon post-deposition annealing. This distinctive difference between the two processing methods can potentially cause, in the latter case, formation of perovskite material with an undesired composition, hence bandgap, particularly in point-source evaporator designs [12], posing a greater challenge for obtaining uniform films as compared to line-sources. Note that in recent studies experiments have been performed where multiple precursors are mixed together beforehand and evaporated from a single source [13, 14].

A major challenge encountered by various groups in the evaporation-based processes is the reproducible fabrication of the perovskite films, even though using the same recipe [15]. The amount of organic cations incorporated into the film usually cannot be precisely controlled [16] merely based on its precursor component recorded evaporation rate or due to its degradation [17]. Apart from sensitivity to the surface properties of the substrate [18], this could also be due to the constraints imposed by the internal design of the evaporation chambers. In point-source thermal evaporation chambers dedicated to large-area substrates, spatially uniform depositions require a relatively long distance between the sources and the substrate holder. When performed in co-evaporation mode, where all the sources are active simultaneously, due to their lower mean free path, it is possible that the organic halides in the vapor phase collide and react with each other or with other precursors, for instance with PbI_2, prior to reaching the substrate surface. Further, it has been observed that under high vacuum conditions organic halides, such as formamidinium iodide (FAI), decompose and transform into other molecules (e.g., s-triazine rings) [19, 20]. These can then make incorporation of precise amount of organic components into the absorber's crystal structure challenging, altering its bandgap and/or causing formation of multiple perovskite phases.

One approach to mitigate these challenges is to deploy *sequential* evaporation instead of co-evaporation. This has become an increasingly popular approach successfully implemented in various ways [21–25]. In one common practice, to improve controllability of the organic halide (e.g., FAI) incorporation into the absorber, the precursor is separately deposited on top of the co-evaporated inorganic precursors. Since only its thickness matters, this makes the fabrication process independent of the evaporation rate of the organic halide, which is known to be prone to rate fluctuation, as long as the organic component is not degraded at higher evaporation rates. Using this sequential evaporation approach, scientifically published PCE values higher than 24% for SJ devices with low absorption threshold of about 1.55 eV have been reported [21, 26], with the remarkable certified efficiencies of 26.21 and 24.88% on 0.1 and 1.0 cm^2 active areas, respectively, achieved by Zhou et al. using a novel hole transport layer (HTL) [26]. Alternatively, to enhance the intermixing of the constituent elements, the individual precursors can be deposited alternately one layer after the other [27], which can be also done in multiple cycles to increase the effective thickness while maintaining high elemental mixing as reported recently by Yan et al. [28]. Moreover, PCEs as high as 18.5% were reported on devices with absorber composition of $Cs_{0.15}FA_{0.85}PbI_{2.85}Br_{0.15}$ with an optical bandgap of about 1.57 eV where $PbCl_2$ was introduced to enhance the absorbers crystallinity and optoelectronic quality [28].

Here, first, we introduce a simple method to obtain initial estimates for the evaporation rates and thicknesses of the precursors used to form perovskite absorber in our point-source and large-area thermal evaporator in a sequential deposition manner. Through deposition of a relatively thick FAI sub-layer onto the self-assembled monolayer (SAM) HTL underneath the co-evaporated inorganic precursors (PbI_2, $PbBr_2$, and CsI) a good batch-to-batch consistency in the optical properties of the wide bandgap absorber is realized. Complete conversion of the precursors into α-perovskite phase required another FAI layer on top to sandwich the co-evaporated inorganic layer. The optical properties of the perovskite films fabricated using the best-known recipe showed very low inhomogeneity of <0.3% across an area equivalent to half M6 (166 × 166 mm) wafer size, making the approach industrially appealing. Device performances over the same area as well as across multiple batches are presented and discussed.

2 | Rate Optimization

A straightforward method is introduced to obtain a reasonable combination of rate values for the precursor materials to form perovskite films with a desired optical bandgap, which can subsequently be further fine-tuned. While the methodology is demonstrated here for the case where four precursor sources (PbI_2, CsI, $PbBr_2$, and FAI) are used so to achieve a wide-bandgap perovskite absorber, relevant to monolithic perovskite-silicon tandem cells, this approach can be adapted for any number of point or linear sources and any perovskite composition.

First, an initial rate combination of the precursors is calculated such that a stoichiometric composition of the perovskite of interest can be theoretically realized. This rate combination is then used to co-evaporate the sources simultaneously onto a substrate in a static mode for which the substrate holder remains stationary, that is, without rotation. The static deposition results in gradients in the composition of the deposited film potentially giving access to regions where perovskite composition of interest with the appropriate optical bandgap and electronic properties is

formed, as well as regions without the desirable perovskite structure and composition. The total thickness of the layer is limited by one of the sources.

Next to this, individual precursors are evaporated one at a time on separate substrates, again in a static mode, at a similar set rate as for the static co-evaporation process. The individual layer thickness can be set to the value recorded by the quartz crystal microbalances (QCMs) in the initial co-evaporation process of all sources. Such static mode deposition results in a gradient of thicknesses across the substrate (see Figure 1A–C; pseudo-square crystalline silicon, c-Si, wafer; see Figure S1). The thickness distributions were obtained using spectroscopy ellipsometry (SE) mapping. For the total deposition time, the thickness gradient translates into gradient of rates across the substrate for each individual precursor.

Photoluminescence (PL) imaging technique is then used to find the regions across the statically deposited and converted film where the PL emission at the desired peak emission energy is highest and does not show a double peak emission from segregated regions. The corresponding coordinates of the region with the strongest, uniform PL emission intensity are identified and subsequently located on the statically deposited single layers on which average rates can be calculated. These newly selected rates are then used to perform co-evaporation of all the precursor sources in a dynamic mode (i.e., substrate rotating) to deposit a perovskite absorber with an ideally homogeneous, optimized composition, and optical bandgap energy across the substrate.

For the reasons mentioned earlier we adopted a sequential evaporation approach in which FAI is evaporated separately from the inorganic precursors. Therefore, the above-explained rate optimization procedure needed to be modified accordingly. In this work, for the rate optimization procedure, FAI of various thicknesses was first deposited in a dynamic evaporation mode onto the HTL (here, MeO-2PACz) covered indium-doped tin oxide (ITO)-glass substrates. Afterwards, the three inorganic precursors were co-evaporated in a static mode. In this sequential deposition rate optimization approach, the amount of FAI required to form the perovskite composition of interest is controlled via its thickness variation but not a gradient of its thickness, as explained above. After the deposition the layers were annealed at 180°C for 5 min on a hotplate in a glovebox (N_2) environment [18] (see Note S1 and Figure S2 in the Supporting Information). Note that this sequence where FAI is deposited underneath

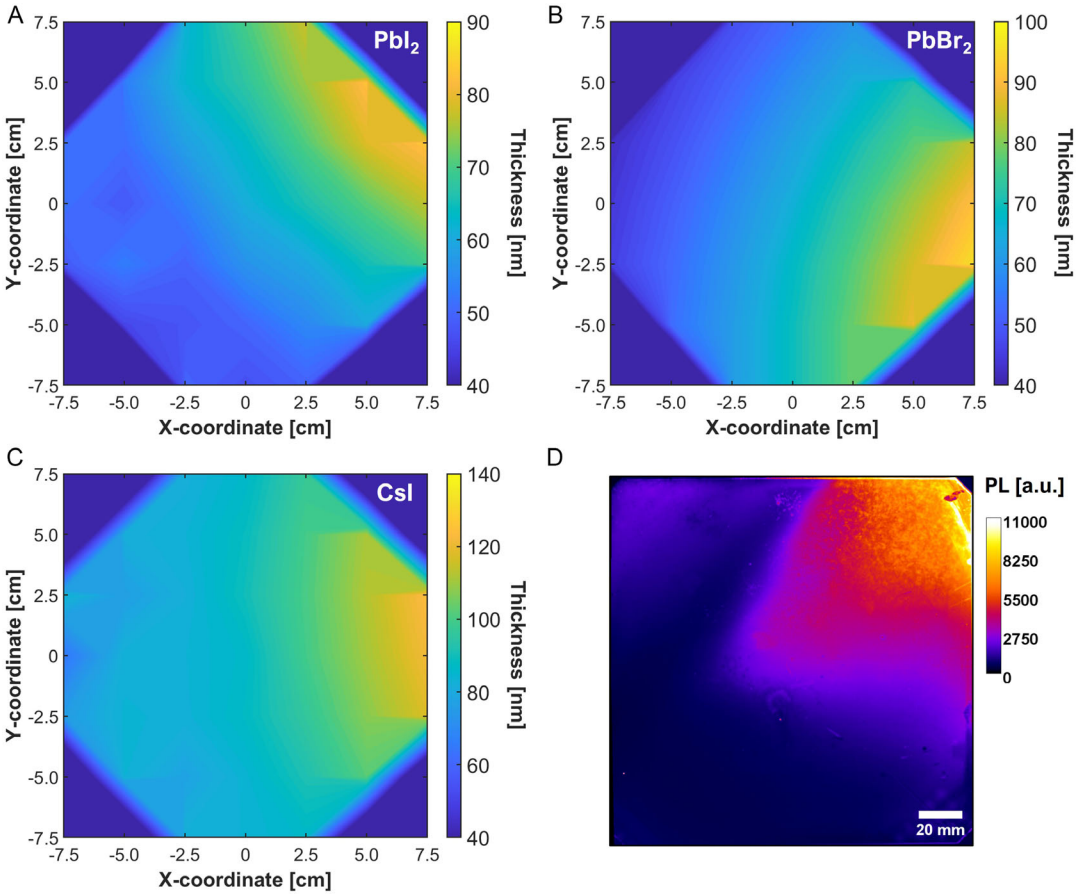

FIGURE 1 | Spatial thickness variation of the individual precursor layers, (A) PbI_2, (B) $PbBr_2$, and (C) CsI, deposited in a static mode with no substrate rotation. Thicknesses were obtained by fitting the optically transparent range of the measured spectroscopy ellipsometry spectra. Note that the single layers were deposited onto pseudo-square M6 size c-Si wafers and therefore, the farthest coordinate close to the uncut, round, corners on which thickness was measured was restricted to those 5 cm off the axes so to also avoid being too close to the edge of the wafer for the SE measurements. (D) PL image of an evaporated (dynamic FAI and static inorganics) and subsequently annealed film acquired using BP740−10 filter at the detection side. Light-emitting diodes with central wavelength of 525 nm was used as the illumination source.

the co-evaporated inorganic precursors was initially adapted to potentially have a better control over the amount of FA^+ available for incorporation into the perovskite structure by preventing the loss of the organic element during the relatively high-temperature annealing process. Three bottom-FAI thicknesses were tested, 225, 175, and 125 nm, of which the latter resulted in the overall highest PL emission intensity detected using a bandpass filter with center wavelength of 740 nm (~1.68 eV) and bandwidth of 10 nm (denoted as BP740−10). The PL image of the sample with 125 nm thick FAI is shown in Figure 1D. The rates obtained using this method are about 0.81, 0.25, and 0.40 Å/s for PbI_2, $PbBr_2$, and CsI, respectively. These rates are used in the following sections in a dynamic deposition mode for perovskite film fabrication combined with 125 nm bottom-FAI deposited at a rate of 1.0 Å/s. It is important to note that these evaporation rates are the ones measured on the QCMs but not the true evaporation rate of individual precursor at the substrate surface.

Finally, uniform deposition of the FAI on a large substrate (M6 wafer here) in a dynamic mode – as in the presented rate optimization procedure – has the added advantage of eliminating the need to map its thickness gradient. The latter is required if FAI is deposited in a static mode for a co-evaporation process rate optimization. Such thickness mapping requires long measurement times, even when automated SE technique is used, and is generally performed in ambient. Throughout such long measurement times, the FAI quality and morphology can change, making proper thickness determination of this organic-based layer a challenge prone to large uncertainties.

3 | Structural and Optical Characterization of the Perovskite Absorber

Using the processing parameters obtained through the procedure described in the previous section, FAI and co-evaporated inorganic precursors were sequentially evaporated onto SAM-covered ITO substrates and subsequently annealed at 180°C for 5 min on the hotplate in a nitrogen-filled glovebox to form the perovskite film. The PL peak emission is at ~1.7 eV (Figure S3), which in this work is simply denoted as the absorption threshold or optical bandgap of the absorber. While this peak emission energy still lies within the detection range of the BP filter used above in the rate optimization procedure, it is at the higher energy end, at shorter wavelengths than that of the filter's cut-on wavelength, making it a less likely emission being detected in Figure 1D. This discrepancy between the dominant PL emission peak energy detected in the rate optimization procedure (Figure 1D) and here could partly be due to the fact that in the previous section the underlying surfaces onto which the layers were deposited were different; FAI-covered substrate in Figure 1D onto which the inorganic precursors were co-evaporated statically, whereas the individual inorganic precursors, as shown in Figure 1A–C, were deposited on native oxide covered c-Si wafers. Therefore, the identified rates from Figure 1A–C based on the coordinates identified from Figure 1D could result in slightly different composition compared to that of the latter.

While no peculiar features were observed in the optical response of the fabricated absorber (see Figure S3), the 1D X-ray diffraction (XRD) measurement results indicate the presence of a secondary phase in the film, identified at around $2\theta = 11.2°$ (Cu-K_α), which can be clearly seen in Figure S3. This phase is dominant in the as-deposited film, and its diffraction peak intensity reduces upon annealing (Figure S3). To have a closer look into the evolution of the phases, 2D XRD measurements in grazing incidence geometry were performed in-situ during annealing. The 1D XRD patterns were obtained by azimuthally integrating the 2D diffraction patterns (see Note S3 for details on the data treatment). A section of the 1D diffractograms acquired at room temperature before starting the annealing and after annealing at 180 °C for 4 min and 30 s is shown in Figures 2A and 2B, respectively (the complete diffractograms are shown in Figure S4).

Figure 2A shows a reflex at $2\theta = 14.2°$ (Cu-K_α) which is attributed to the perovskite phase. The measured diffractogram shows the same reflexes as the cubic α perovskite phase [29] (Figure S4). The α-perovskite can have a mixture of FA and Cs on the A-site and/or a mixture of Br and I on the X-site. Furthermore, the reflex at $2\theta = 11.2°$ (Cu-K_α) is attributed to the 002 reflex of a

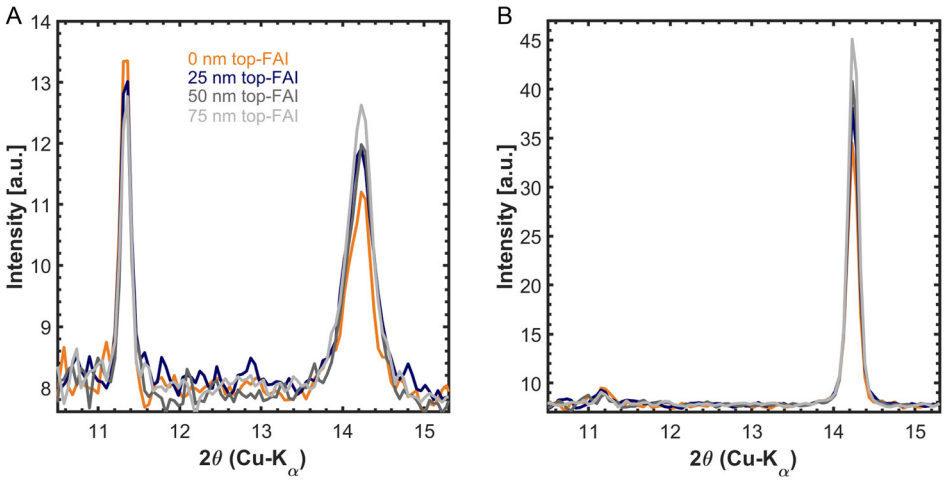

FIGURE 2 | 1D diffractograms azimuthally integrated from a 2D diffraction pattern at an incidence angle of 8°. Results are for four different top-FAI thicknesses measured (A) at room temperature before starting the annealing process and (B) at 180°C 4 min and 30 s into annealing.

secondary AB_2X_5 phase. Its Bragg angle lies between that of the 002 reflexes of $CsPb_2Br_5$ and $CsPb_2I_5$ [30, 31].

Stoichiometric addition of the three inorganic precursors results in $CsPb_2(Br_{0.4}I_{0.6})_5$. Using Vegard's law for orthorhombic crystals - as explained in Supplementary Information Note S3 - an approximate concentration of $(Br_{0.4}I_{0.6})$ can be estimated from the position of the 002 reflex. A calculated diffraction pattern with this halide ratio gives good agreement with all observed reflexes of the secondary phase, as shown in Figure S5. With these findings, it is proposed that the secondary phase is the purely inorganic $CsPb_2(Br_{0.4}I_{0.6})_5$.

The XRD pattern acquired at a sample temperature of 170°C after 4 min and 30 s of thermal annealing (Figure 2B) shows the same two reflexes, as observed in Figure 2A, but with an increased intensity of the α-perovskite peak and a reduced intensity of the secondary phase. The evolution of the relation of the reflex intensity from the secondary phase in comparison to that of the α-perovskite phase has been analyzed in Figure S6. It shows that after annealing the amount of the secondary phase is significantly reduced in comparison to the α-perovskite. Most of the intensity changes take place within the first minute of annealing.

To improve the conversion of the deposited precursors to α-phase perovskite, the fabrication process was slightly modified, introducing an additional FAI layer evaporated on top of the co-evaporated inorganic layer (called top-FAI here on). The schematic of this three-step sequential evaporation process is illustrated in Figure 3. A series of top-FAI layer thicknesses were tested from 0 to 75 nm with 25 nm intervals. All samples had 125 nm thick bottom-FAI deposited onto the spin-coated MeO-2PACz covered ITO glass followed by co-evaporated inorganic halide salts (i.e., PbI_2, $PbBr_2$, and CsI). Exemplary data showing the change in the evaporation rates and thicknesses over the course of a deposition for all the four precursors are provided in Figure S7.

Increasing the top-FAI thickness in steps of 25 nm from 0 up to 75 nm increases the intensity of the perovskite diffraction reflex before, during, and after annealing, as presented in Figure 2. Indeed, it also lowers the amount of secondary phase in comparison to the α-perovskite phase as illustrated in Figure S6. However, in-situ experiments show that after 5 minutes of annealing the secondary phase does not disappear completely even for a top-FAI layer thickness of 75 nm.

The existence of a larger proportion of perovskite can be explained by the fact that more FAI is available for the conversion of the inorganic components to perovskite. In addition, it may be advantageous that the FAI is not only below the inorganic components, but also above them. The top-view scanning electron microscopy (SEM) images in Figure S8 show that the amount of visible perovskite increases with increasing the top-FAI thickness. The secondary electron beam SEM images show regions of two different average atomic number. From the in-situ XRD experiments, we detected two different crystalline phases too. Hence, we speculate that bright regions in Figure S8 are the inorganic $CsPb_2(Br_{0.4}I_{0.6})_5$ phase and the dark regions are the perovskite.

The morphology of the films processed with the four different top-FAI thicknesses was assessed using cross-sectional SEM imaging. Example cross-sectional SEM images are shown in Figure 4. Images with a wider field of view are given in Figure S9 supporting our observations as discussed in the following.

Overall, the perovskite film thicknesses are in the range of 400–450 nm. It can be seen that as the FA^+ content in the absorber is increased through increasing the top-FAI layer thickness, the perovskite layer becomes more similar to the typically reported polycrystalline perovskite films with large columnar apparent grains reaching though the entire film thickness. The film without any top-FAI did not form clear grains upon annealing, particularly closer to the surface of the film. By introducing 25 nm top-FAI, visible grains seem to emerge from the top and the bottom of the film forming a horizontal boundary line. This boundary line disappears as the amount of top-FAI is thickened up to 50 nm for which grains grow throughout the entire layer thickness. This indicates the necessity of adding sufficient top FA^+ cations for a homogeneous interdiffusion across the absorber. A more distinctive polycrystalline film is realized as the top-FAI thickness is increased to 75 nm, with clear columnar grains. As will be shown in the following sections, this latter film with apparently more desirable morphology and higher degree of

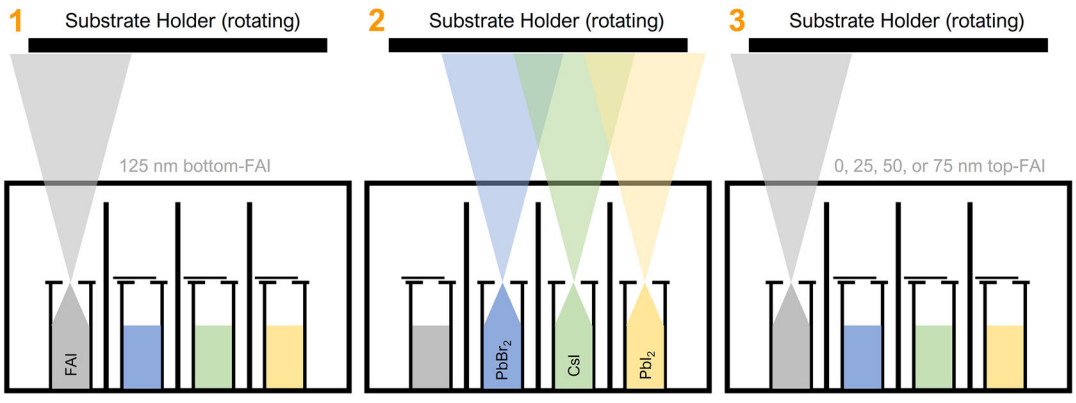

FIGURE 3 | Schematic of the processing steps. In the first step, 1, 125 nm FAI bottom layer is deposited on the SAM-covered ITO glass onto which the inorganic precursors are co-evaporated in the second step, 2. The layers are finally capped with a thinner FAI top layer in step 3 with various thickness ranging from 0 to 75 nm.

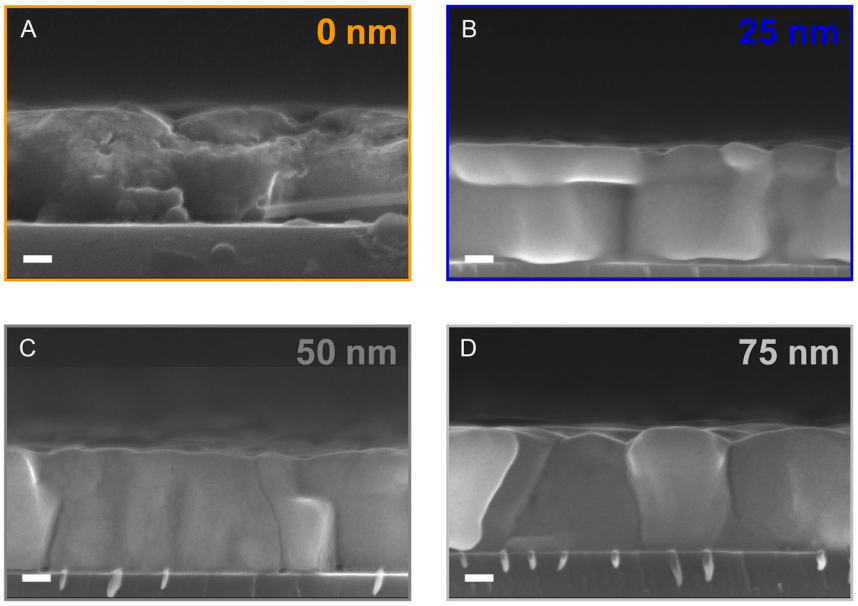

FIGURE 4 | Cross-sectional SEM images of the perovskite films fabricated with (A) 0, (B) 25, (C) 50, and (D) 75 nm top-FAI. The scale bar in all the images is 25 nm.

crystallinity – observed in the XRD results – does not necessarily lead to a high-quality absorber with reduced charge-carrier recombination nor giving the best performing solar cells among the four perovskite layer combinations investigated here. We speculate that this is partly due to the presence of excessive amount of FA^+ in the absorber, mostly toward the electron extracting stack, hindering charge extraction out of the high crystallinity perovskite absorber.

To evaluate the absorber quality, absolute PL spectra were acquired on these samples. The evolution of the PL peak emission energy at 1.7 ± 0.01 eV for all layers over 60 s under continuous green laser illumination is shown in Figure 5A. Although not measured for very long duration, these results provide an initial insight into the compositional photo-stability of these perovskite films when interfaced with a hole selective contact only (the normalized PL spectra are given in Figure S10). The changes in the implied-V_{OC} (iV_{OC}), calculated based on the measured PL quantum yield (PLQY) values (Figure S11), over the same time period are plotted in Figure 5B. While a transient response can be seen in the iV_{OC} of all the samples, films with zero and 75 nm top-FAI showed the highest and the lowest values, respectively, and absorbers with 25 and 50 nm top-FAI showed comparable iV_{OC} values, starting at values equal to or higher than 1200 mV. A similar trend in the average device V_{OC}s was also observed (see the next section).

4 | Integration into SJ Solar Cells

Devices were then fabricated from the half-stacks with sequentially evaporated perovskite absorbers with various top-FAI thicknesses. The solar cells have the following structure, glass/ITO/MeO-2PACz/perovskite/C_{60}/bathocuproine (BCP)/Ag, as illustrated in Figure 6A, all layers being processed on 25×25 mm substrates (except for the Ag pattern). On each substrate 6 metalized cells are formed, each with an active area of 0.16 cm^2. The summary of the resulting light current density–voltage (J–V) measurement parameters is presented in Figure 6B–E. It should be noted that the statistics on the measurement data were calculated on the cells with fill factor (FF) higher than 50% in the reverse (V_{OC} to short-circuit current, J_{SC}) J–V scan.

For almost all the processing conditions with different top-FAI thicknesses, a voltage deficit of about 100 mV with respect to the average iV_{OC} results (Figure 5C) was observed in the average V_{OC} of the finished solar cells (Figure 6B). It should be noted that the light J–V curves were measured under 1-Sun intensity, whereas the PLQY data were acquired under approximately 0.5 Suns equivalent photon flux, indicating an even larger voltage deficit. While thermally evaporated perovskite absorbers are considered to have larger bulk non-radiative recombination losses compared to their solution-processed counterparts [32], it seems the observed large voltage loss in the devices is also partly originating from the increased recombination activity upon perovskite/C_{60} contact formation, which is not uncommon [33]. Further, the V_{OC} trend with respect to the top-FAI thickness is similar to that of iV_{OC}s' (see Figure S12), indicating the possible contribution from other dominant factors to the voltage losses in the devices than just the increased recombination activity at the perovskite/C_{60} interface.

When it comes to FF, the highest median FFs were measured on the devices made by 50 nm top-FAI, slightly higher than those without top-FAI and greater than samples receiving 25 and 75 nm top-FAI. Nevertheless, the average FF for the 0 and 50 nm top-FAI devices was comparable. Similar trend, though with different absolute values, was repeatedly realized in other processed batches (see Figure S13). A noticeably lower FF of the devices with 75 nm top-FAI compared to those with 50 nm top-FAI could be due to the energetic misalignment formed between the organic element-rich surface of the perovskite layer and C_{60}.

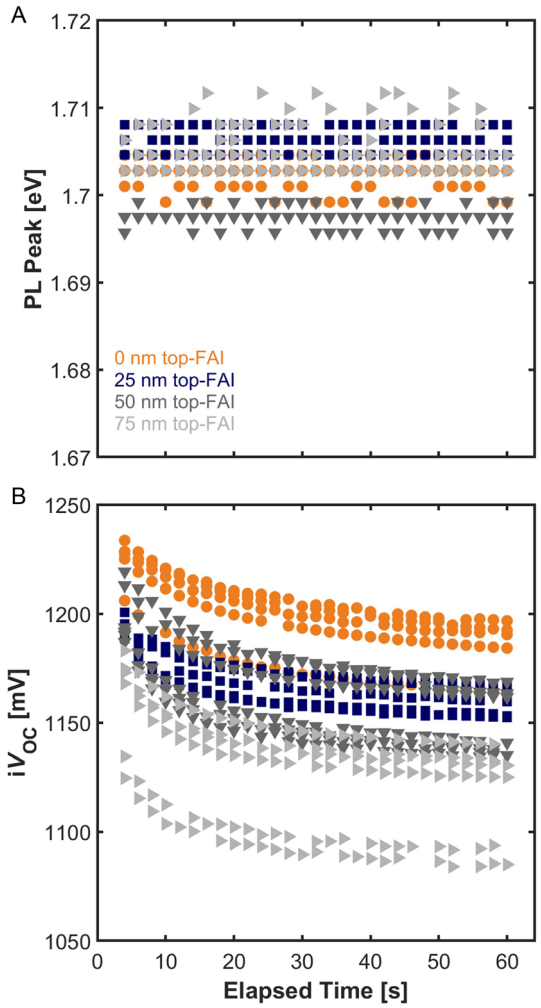

FIGURE 5 | (A) PL peak emission energy, interpreted as the optical bandgap of the absorber, measured as a function of time over 60 s using a 520 nm laser with approximately 0.5 Suns equivalent photon flux. (B) Time-evolved implied-V_{OC} measured under approximately 0.5 Suns equivalent photon flux on the four sample types with different top-FAI thicknesses.

The power output of the best-performing cells from the four different processing conditions (i.e., top-FAI thicknesses) was tracked for 180 s, measured under nitrogen-filled environment, and the results are presented in Figure 6F. It is interesting that while the highest stabilized power output within this time length was obtained for the devices with 50 nm top-FAI, the device without top-FAI did not show significant difference and approached the same values toward the end of the measurement. This is unexpected considering the morphological (SEM) and structural (XRD) analysis discussed in the previous sections. While further study is required to understand this observation, it is possible that the real impact of the differences in crystallinity and morphology of these two absorbers can be only revealed when stability is assessed for longer durations and under operational conditions. A longer maximum power point (MPP) tracking measurement over 10 min was further performed on a device with 50 nm top-FAI with a PCE of 16%, given in Figure S14.

We further compared the demonstrated three-step sequential evaporation of this work with the more commonly practiced method where the inorganic precursors are first (co-)evaporated onto the contact layer on top of which the organic halide salt is subsequently evaporated [34]. Three different top-FAI thicknesses were tested in the latter approach that were chosen to be at least equal to the sum of the bottom- and top-FAI thicknesses of the three-step sequential evaporation method. In order for the samples to experience the same processing conditions, as much as related, the co-evaporated inorganic precursor layers for all the samples were processed in one deposition run, both those fabricated via the three-step sequential evaporation route incorporating bottom-FAI as well as the devices processed via the common, two-step sequential evaporation approach. The results of this comparative study are provided in Figure S15, indicating noticeably higher PV performances for our three-step sequential evaporation method and even for the two-step process where the organic precursor, FAI, is deposited first. While further investigation is required, it is possible that this is due to a low-porosity inorganic scaffold formed when inorganic precursors are co-evaporated first onto the flat HTL surface.

5 | Reproducibility

For a perovskite-based device fabrication process to become industrially relevant it is essential for its reproducibility to be evaluated. Several batches of SJ perovskite solar cells (PSCs) were processed using the three-step sequential evaporation method introduced in the above, all with 50 nm top-FAI layer. The PV parameters across these batches are summarized in Figure 7. Note that the number of substrates, hence solar cells, fabricated in each batch can differ.

The average FF for the reverse and forward *J*–*V* scans are slightly greater than 70% and about 65%, respectively, while the average V_{OC} for both scan directions is about 1075 mV. The spread in the measured FF (calculated based on the standard deviation values of each batch) for the reverse (forward) scan direction is about 12% (17%) and about 47 mV (52 mV) for the V_{OC}, which requires further narrowing down. Such variation extent in the results could originate from different silver pastes applied on the electrodes across the batches for contacting improvement, misalignment between the top and bottom contacts due to shadow mask positioning, reducing J_{SC}, small-area pixel design of the devices, change in the C_{60} quality across the batches [35], and possibly due to the individual layer thickness inhomogeneity since the substrates are randomly located across an M6-equivalent size substrate holder (see Figure S16) throughout the different steps of the evaporation processes. The latter can affect the elemental content within the bulk and at the surface of the absorber affecting the device parameters, hence contributing to the scattered data observed in each processed batch. Higher iV_{OC} values were measured on the films deposited on the HTL compared to the final device V_{OC} values, with average voltage loss of at least 120 mV (Figure 7B). This indicates that improvement in the voltage should be possible through perovskite/C_{60} interface passivation.

Reporting performance reproducibility of PSCs particularly when the absorber is processed using thermal evaporation techniques

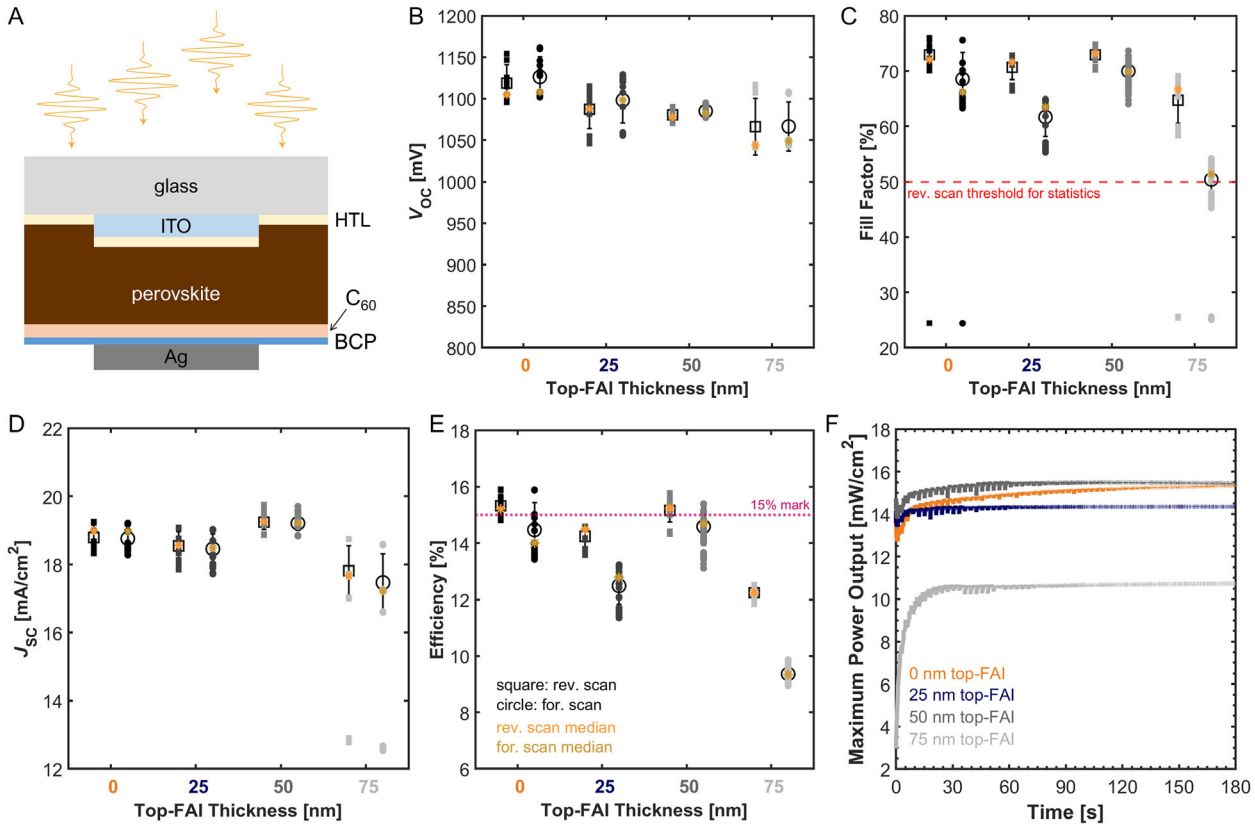

FIGURE 6 | (A) Schematic of the p-i-n device configuration. Summary of the PV parameters extracted from the light *J–V* curves measured on the cells fabricated using various top-FAI thicknesses: (B) V_{OC}, (C) FF, (D) J_{SC}, and (E) power conversion efficiency. Note that the statistics of the PV parameters for both *J–V* scan directions are calculated for devices where their corresponding FF in the reverse scan is greater than 50%. (F) Maximum power point tracking for 3 min under 1-Sun intensity of the best working solar cells of the four different sample types with different top-FAI thicknesses. All the presented measurements are performed in glovebox under nitrogen-filled environment (O_2 and $H_2O < 0.1$ ppm).

is essential [15, 18, 21]. Therefore, it is important that the reported reproducibility results in the literature using sequential evaporation are discussed and compared with the three-step sequential evaporation approach developed in this work. In a noticeable study, Li et al. presented a chlorine-mediated two-step sequential evaporation method in which the inorganic precursors, PbI_2, $PbCl_2$, and CsI, were first co-evaporated onto which FAI was subsequently deposited [21]. While reproducible PCEs higher than 20% were reported over 10 batches, we hesitate a direct comparison of these results with that of our three-step sequential evaporation method due to the compositional differences with much wider bandgap of the absorber layer in the latter (~1.70 eV vs. 1.55 eV), containing bromine too. To the best of the authors' knowledge, this work of Li et al. [21] is the only study which publicly reported performance reproducibility on several batches of their sequentially evaporated devices.

6 | Spatial Uniformity over Large Area Deposition

Here, we show test results of our sequential evaporation process on inch-by-inch substrates which fit into our M6-equivalent size substrate holder (see Figure S16). For this, a batch of 18 half-stack (perovskite/MeO-2PACz/ITO-glass) samples was processed using the recipe with 50 nm top-FAI all in one run, covering an area equivalent to half M6 wafer. On these unfinished devices, PLQY measurements were performed to evaluate the optical properties of the absorber. Next, these same half-stacks were turned into SJ solar cells on which light *J–V* measurement was performed.

Excellent spatial uniformity of the optical properties of the absorber was realized both for the optical bandgap (Figure 8A), being the PL peak emission energy, and the iV_{OC} (Figure 8B) with 0.16% and 0.24% inhomogeneity, respectively, and average values of 1.70 eV and 1230 mV. The corresponding SJ devices showed average V_{OC} of ~1040 mV, for both *J–V* scan directions, and FF of ~74.1% (~70.7%) in reverse (forward) scan direction. The FF map of the median values (median of 6 pixels on each substrate) measured in reverse scan is shown in Figure 8C. Relatively low spatial inhomogeneity of <1.5% and <5% was measured for V_{OC} and FF, respectively, regardless of the *J–V* scan direction. The non-uniformity is calculated according to the following equation, [(max. − min.) × 100/(max. + min.)]. Note that the *J–V* parameters presented in these maps are filtered for devices with FF greater than 50% in the reverse *J–V* scan (102 out of 108 total cells of 0.16 cm^2 each). The scatter plot showing the correlation between the V_{OC} and FF of all the cells is shown in Figure 8D, showing a narrower distribution for the reverse scan data as opposed to the forward scan results. The maps of the rest of the PV parameters are shown in Figure S17.

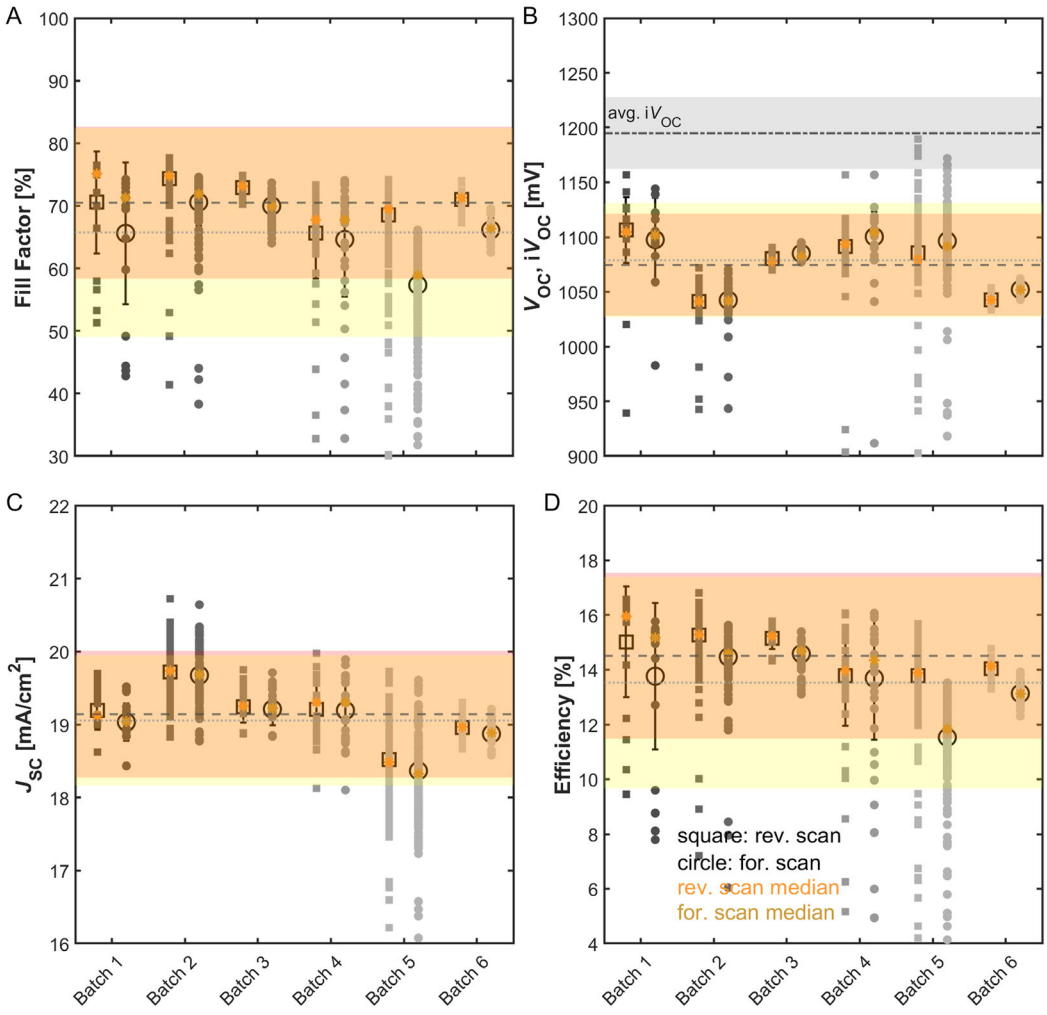

FIGURE 7 | Reproducibility of the SJ solar cell parameters across six batches: (A) FF, (B) V_{OC}, (C) J_{SC}, and (D) power conversion efficiency. Devices are fabricated using the recipe in which the inorganic layer is sandwiched between 125 nm bottom-FAI and 50 nm top-FAI. The dashed and dotted lines in each plot indicate the average value of the corresponding parameter across all the batches for the reverse and forward *J*–*V* scans, respectively. The red and yellow shaded areas show the uncertainty in the measured parameters across all the batches for the reverse and forward scans, respectively. Note that the statistics of the PV parameters for both *J*–*V* scan directions are calculated for devices where their corresponding VOC in the reverse scan is greater than 1000 mV. Also plotted in panel B is a dash-dotted line indicating the mean iV_{OC} value across the batches measured on the unfinished stacks (i.e., without C_{60}, BCP, and metallization) in each batch (measured under 0.5-Suns equivalent photon flux as opposed to the *J*–*V* scans being measured at 1-Sun). These iV_{OC} values were acquired after 4 s of illumination, noting the transient response of the perovskite films to continuous photo-excitation, as shown in Figure 5. The shaded area represents the uncertainty in iV_{OC} measured across the batches.

7 | Integration into Perovskite/Silicon Tandem Solar Cell

Finally, we integrated this three-step sequential evaporation process, with 50 nm top-FAI recipe, into a perovskite/silicon tandem solar cell with industrial, textured bottom-cell. To achieve a conformal coverage of the textured bottom-cell, a geometrical factor of 1.7, as usually used for random pyramids, was adopted to increase the total thickness of the perovskite absorber. This factor was taken into account for all the three separately evaporated layers (bottom-FAI, co-evaporated inorganic precursors, and top-FAI), resulting in an average perovskite thickness of ~600 nm (as opposed to the ~400 nm absorber in the SJ solar cells). Details of the tandem cell fabrication processes are provided in Note S1 of the Supporting Information. The cross-sectional SEM images of a tandem cell before annealing and after conversion of the perovskite layer are presented in Figure S18. A compact absorber conformally following the silicon texture with observable grain boundaries upon annealing can be seen.

An example of *J*–*V* curve of the best-performing tandem cell is shown in Figure S19. The expected V_{OC} of the tandem device, derived by summing the average V_{OC} values for the individual SJ cells (0.70 ± 0.01 V for our 250 μm thick FZ-Si based heterojunction bottom-cell at 0.5 Suns and 1.07 ± 0.06 V for the top-cell as was derived above), is approximately 1.74 ± 0.06 V. However, the measured V_{OC} of 1.62 V (see Figure S19) is 120 mV lower, indicating additional voltage losses upon combining the two cells into a tandem configuration. The notable modification in this configuration is the conformally deposited perovskite layer covering the textured silicon sub-cell. This additional voltage loss can be partly attributed to the increased surface-to-volume ratio, which will result in higher surface

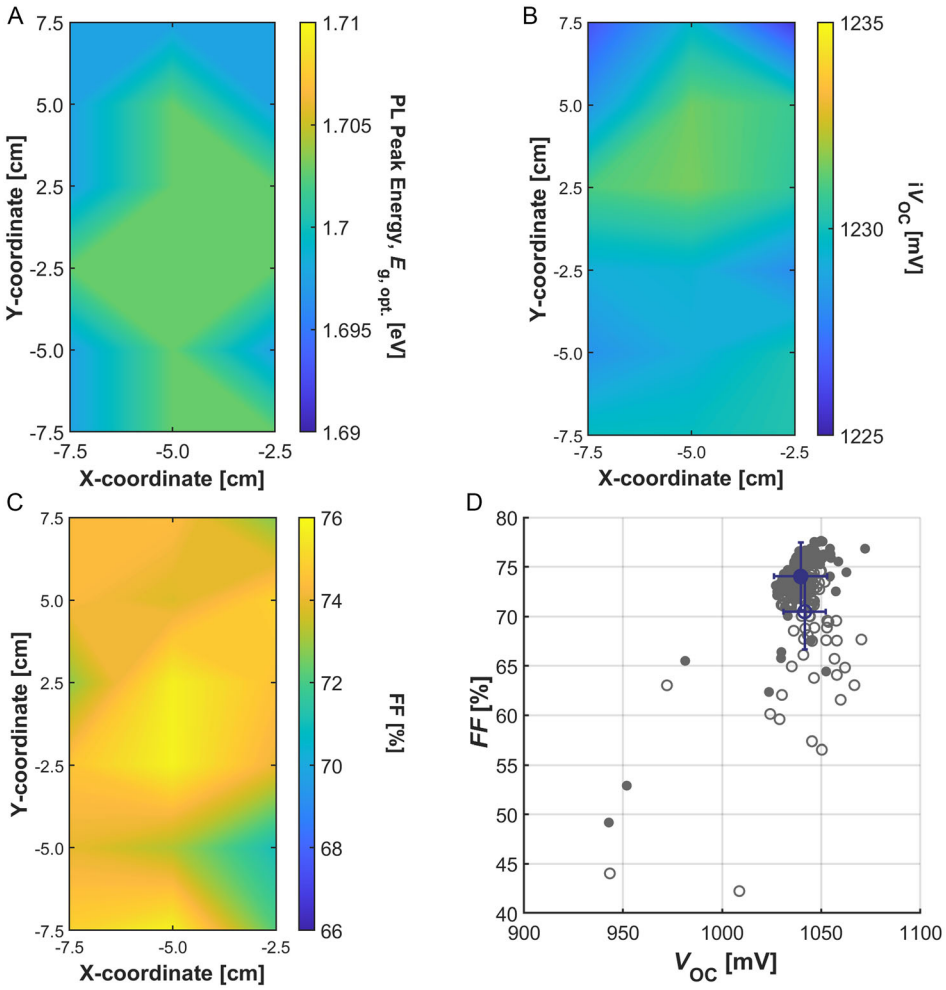

FIGURE 8 | (A) PL peak emission map, denoted as the optical bandgap, and (B) implied-V_{OC} map, measured under approximately 0.5-Suns equivalent photon flux from the glass side, plotted as a function of the location on the sample holder. Important note: the maps are constituted from the results measured on 18 substrates, each accommodating 6 device pixels of 0.16 cm^2 area, covering *half* of an area equivalent to M6 size wafer. (C) Map of the median FF values (median of 6 pixels/cells on each substrate). These devices were fabricated using the half-stacks on which PLQY measurements were performed and presented in panels A and B. (D) Scatter plot of device FF versus V_{OC} measured on 108 small-area cells. Filled (hollow) symbols represent the reverse (forward) scan measurement results.

recombination losses. Due to the top-cell limitation, FF and J_{SC} are mostly dominated by that of the perovskite sub-cell. Moreover, the front electrode is different comprising an SnO_2 buffer layer (deposited using Atomic Layer Deposition technique) and a sputtered indium-doped zinc oxide in the tandem cells compared to BCP/Ag for the SJs. This might lead to additional voltage losses due to the deposition-induced damage.

8 | Conclusions and Next Steps

We demonstrated, using a sequential evaporation method for wide-gap perovskites, suited for incorporation in perovskite/silicon tandem cells, promising potential for scalable fabrication of perovskite-based solar cells, offering consistent device performance across several batches and with high spatial uniformity. We attribute these, at least in part, to the inclusion of an FAI bottom layer (between the HTL and the inorganic layer), which plays a stabilizing role during film formation. Moreover, the presence of FAI both beneath and on top of the co-evaporated inorganic can assist interdiffusion, hence uniform structural conversion throughout the absorber.

The main limiting parameters in the devices fabricated using the sequential evaporation approach developed here are open-circuit voltage and to a lesser extend FF. Further improvements in solar cell parameters, particularly in the open-circuit voltage, and consequently the FF, are expected through incorporation of an appropriate interface passivation layer [36, 37] as well as additives into the bulk absorber [38, 39] to mitigate non-radiative recombination losses. For this purpose, a range of passivating contact materials and bulky organic halide salts should be screened. Additionally, the presence of the undesirable secondary phase, $CsPb_2(I,Br)_5$, mostly likely still present on the surface of the absorber, must be completely suppressed. Achieving this may require re-optimization of both the deposition rates, hence composition, as well as the annealing conditions, including careful control of the relative humidity during thermal treatment, as demonstrated by other researchers in the field, to promote the formation of the desired perovskite phase. The latter has also been shown to improve device voltage [23].

From an industrial perspective, the sequential evaporation process described here offers compatibility with large-area processing and vapor-phase deposition technologies, which are attractive for high-throughput manufacturing. However, for broader applicability, particularly in tandem configurations with c-Si bottom-cells, process parameters may need to be tailored to accommodate differences in substrate topography and surface properties.

Acknowledgments

The authors gratefully acknowledge financial support by the Helmholtz Association (program-oriented funding phase IV, MTET Topic 1, Code: 38.01.03) and the European Union-funded project PEPPERONI (No. 101084251). The authors further acknowledge the Helmholtz Association for funding provided via the Solar Technology Acceleration Platform (Solar TAP) and the "Zeitenwende" project. Additional funding was provided by the German Federal Ministry for Economic Affairs and Climate Action (BMWK) through the KOALA (03EE1041), KOALA-PLUS (03EE1109A), PeroQ2 (03EE1183B), and the SHAPE (03EE1123 A-E) projects. Views and opinions expressed are, however, those of the authors only and do not necessarily reflect those of the European Union or the European Climate, Infrastructure and Environment Executive Agency (CINEA). Neither the European Union nor the granting authority can be held responsible for them.

Conflicts of Interest

The authors declare no conflicts of interest.

Data Availability Statement

The data that support the findings of this study are available from the corresponding author upon reasonable request.

References

1. T. Abzieher, D. T. Moore, M. Ross, et al., "Vapor Phase Deposition of Perovskite Photovoltaics: Short Track to Commercialization?," *Energy & Environmental Science* 17, no. 5 (2024): 1645–1663, https://doi.org/10.1039/D3EE03273F.

2. M. A. Green, E. D. Dunlop, M. Yoshita, et al., "Solar Cell Efficiency Tables (Version 64)," *Progress in Photovoltaics: Research and Applications* 32, no. 7 (2024): 425–441, https://doi.org/10.1002/pip.3831.

3. E. Bellini and V. Shaw, 2025. "*Longi achieves 34.85% Efficiency for Two-Terminal Tandem Perovskite Solar Cell*," Pv Magazine, April 18.

4. P. Jowett, 2024. "*Qcells hits 28.6% Efficiency with Scalable Perovskite-Silicon Solar Cell*," Pv Magazine, December 19.

5. A. S. Subbiah, S. Mannar, V. Hnapovskyi, et al., "Efficient Blade-Coated Perovskite/Silicon Tandems via Interface Engineering," *Joule* 9, no. 1, (2025): 101767, https://doi.org/10.1016/j.joule.2024.09.014.

6. M. R. Leyden, V. Skorjanc, A. Miaskiewicz, et al., "Loading Precursors into Self-Assembling Contacts for Improved Performance and Process Control in Evaporated Perovskite Solar Cells," *Solar RRL* 8, no. 21 (2024): 2400575, https://doi.org/10.1002/solr.202400575.

7. Y. Gupta, M. Heydarian, M. Heydarian, et al., "Photostable Inorganic Perovskite Absorber via Thermal Evaporation for Monolithic Perovskite/Perovskite/Silicon Triple-Junction Solar Cells," *Progress in Photovoltaics: Research and Applications*, 33, no. 7, (2025): 782, https://doi.org/10.1002/pip.3923.

8. J. Yan, J. Zhao, H. Wang, et al., "Crystallization Process for High-Quality $Cs_{0.15}FA_{0.85}PbI_{2.85}Br_{0.15}$ Film Deposited via Simplified Sequential Vacuum Evaporation," *ACS Applied Energy Materials* 6, no. 20 (2023): 10265–10273, https://doi.org/10.1021/acsaem.3c00203.

9. P.-S. Shen, Y.-H. Chiang, M.-H. Li, T.-F. Guo, and P. Chen, "Research Update: Hybrid Organic-Inorganic Perovskite (HOIP) Thin Films and Solar Cells by Vapor Phase Reaction," *APL Materials* 4, no. 9 (2016): 091509, https://doi.org/10.1063/1.4962142.

10. P. S. C. Schulze, K. Wienands, A. J. Bett, et al., "Perovskite Hybrid Evaporation/ Spin Coating Method: From Band Gap Tuning to Thin Film Deposition on Textures," *Thin Solid Films* 704 (2020): 137970, https://doi.org/10.1016/j.tsf.2020.137970.

11. S. Rafizadeh, K. Wienands, P. S. C. Schulze, et al., "Efficiency Enhancement and Hysteresis Mitigation by Manipulation of Grain Growth Conditions in Hybrid Evaporated–Spin-Coated Perovskite Solar Cells," *Acs Applied Materials & Interfaces* 11, no. 1 (2019): 722–729, https://doi.org/10.1021/acsami.8b16963.

12. K. Zhang and R. Faber, "*Linear Thermal Evaporation Source for Large Area CIGS Solar Cell Manufacturing*," 2012, Society of Vacuum Coaters, https://www.svc.org/index.php?src=directory&view=resource_library&submenu=DigitalLibrary.

13. H. Li, L. Tan, C. Jiang, et al., Molten Salt Strategy for Reproducible Evaporation of Efficient Perovskite Solar Cells. *Advanced Functional Materials* 33, no. 10, (2023): 2211232, https://doi.org/10.1002/adfm.202211232.

14. I. Susic, L. Gil-Escrig, F. Palazon, M. Sessolo, and H. J. Bolink, "Quadruple-Cation Wide-Bandgap Perovskite Solar Cells with Enhanced Thermal Stability Enabled by Vacuum Deposition," *ACS Energy Letters* 7, no. 4 (2022): 1355–1363, https://doi.org/10.1021/acsenergylett.2c00304

15. J. Borchert, I. Levchuk, L. C. Snoek, et al., "Impurity Tracking Enables Enhanced Control and Reproducibility of Hybrid Perovskite Vapor Deposition," *ACS Applied Materials & Interfaces* 11, no. 32 (2019): 28851–28857, https://doi.org/10.1021/acsami.9b07619.

16. M. Roß, M. B. Stutz, and S. Albrecht, "*Revealing the Role of Methylammonium Iodide Purity on the Vapor-Phase Deposition Process of Perovskites*," 6, no. 10 (2022): 2200500, https://doi.org/10.1002/solr.202200500.

17. S. Thampy, B. Zhang, J.-G. Park, K.-H. Hong, and J. W. P. Hsu, "Bulk and Interfacial Decomposition of Formamidinium Iodide (HC(NH2)2I) in Contact with Metal Oxide," *Materials Advances* 1, no. 9 (2020): 3349–3357, https://doi.org/10.1039/D0MA00624F.

18. V. Škorjanc, A. Miaskiewicz, M. Ross et al., "Seed Layers for Wide-Band Gap Coevaporated Perovskite Solar Cells: CsCl Regulates Band Gap and Reduces Process Variability," *ACs Energy Letters* 9, no. 11 (2024): 5639–5646, https://doi.org/10.1021/acsenergylett.4c02173.

19. F. Sahli, Q. J.-M. A. Guesnay, N. Salsi, L. Duchêne, C. Ballif, and Q. Jeangros, "*Ammonia-Assisted Vapour Transport Deposition of Formamidinium Salts for Perovskite Thin Films*," 2025, preprint, infoscience, 2021, https://infoscience.epfl.ch/entities/publication/9fe583c0-bc80-4cc1-8877-0b9b59da0b7b.

20. M. Kroll, S. D. Oz, Z. Zhang, et al., "Insights into the Evaporation Behaviour of FAI: Material Degradation and Consequences for Perovskite Solar Cells," *Sustainable Energy & Fuels* 6, no. 13 (2022): 3230–3239, https://doi.org/10.1039/D2SE00373B.

21. H. Li, J. Zhou, L. Tan, et al., "Sequential Vacuum-Evaporated Perovskite Solar Cells with More than 24% Efficiency," *Science Advanced* 8, no. 28 (2022): eabo7422, https://doi.org/10.1126/sciadv.abo7422.

22. N. Rodkey, I. Gomar-Fernández, F. Ventosinos, C. Roldan-Carmona, L. J. A. Koster, and H. J. Bolink, "Close-Space Sublimation as a Scalable Method for Perovskite Solar Cells," *ACS Energy Letters* 9, no. 3 (2024): 927–933, https://doi.org/10.1021/acsenergylett.3c02794.

23. R. A. Nambiar, D. P. McMeekin, M. K. Czenry, et al., "Interdiffusion Control in Sequentially Evaporated Organic–inorganic Perovskite Solar Cells," *EES Solar* 1 (2025): 129, https://doi.org/10.1039/D5EL00017C.

24. M. H. Lee, D. W. Kim, Y. W. Noh, et al., "Controlled Crystal Growth of All-Inorganic CsPbI2Br via Sequential Vacuum Deposition for Efficient Perovskite Solar Cells," *ACS Nano* 18, no. 27 (2024): 17764–17773, https://doi.org/10.1021/acsnano.4c03079.

25. S. Lee, Y. S. Yoon, S. Shafian, J. Y. Kim, and K. Kim, "Sequential Co-Deposition of Perovskite Film: An Effective Way of Tailoring Bandgap in All Vacuum Processed Perovskite Solar Cells," *Small Methods, Apr* (2025), 2500104, https://doi.org/10.1002/smtd.202500104.

26. J. Zhou, L. Tan, Y. Liu, et al., "Highly Efficient and Stable Perovskite Solar Cells via a Multifunctional Hole Transporting Material," *Joule* 8, no. 6 (2024): 1691–1706, https://doi.org/10.1016/j.joule.2024.02.019.

27. K. L. Heinze, T. Schulz, R. Scheer, and P. Pistor, "Structural Evolution of Sequentially Evaporated (Cs, FA)Pb(I, Br)3 Perovskite Thin Films via In Situ X-Ray Diffraction," *Physica Status Solidi A* 221, no.3 (2024): 2300690, https://doi.org/10.1002/pssa.202300690.

28. J. Yan, J. Nespoli, R. K. Boekhoff, et al., "Chloride-Improved Crystallization in Sequentially Vacuum-Deposited Perovskites for p–i–n Perovskite Solar Cells," *Sustainable Energy & Fuels* 9 (2025): 2729, https://doi.org/10.1039/D4SE01744G.

29. A. Marronnier, G. Roma, S. Boyer-Richard, et al., "Anharmonicity and Disorder in the Black Phases of Cesium Lead Iodide Used for Stable Inorganic Perovskite Solar Cells," *ACS Nano* 12, no. 4 (2018): 3477–3486, https://doi.org/10.1021/acsnano.8b00267.

30. M. Li, S. Peng, S. Fang, et al., "Synthesis of Two-Dimensional CsPb2X5 (X = Br and I) with a Stable Structure and Tunable Bandgap by CsPbX3 Phase Separation," *The Journal of Physical Chemistry Letters* 13, no. 11 (2022): 2555–2562, https://doi.org/10.1021/acs.jpclett.2c00116.

31. V. Drushliak and M. Szafrański, "Thermodynamic Stability, Structure, and Optical Properties of Perovskite-Related CsPb2Br5 Single Crystals under Pressure," *Inorganic Chemistry* 61, no. 36 (2022): 14389–14396, https://doi.org/10.1021/acs.inorgchem.2c02253.

32. C. Dreessen, K. P. S. Zanoni, L. Gil-Escrig, et al., "When JV Curves Conceal Material Improvements: The Relevance of Photoluminescence Measurements in the Optimization of Perovskite Solar Cells," *Advanced Optical Materials* 12, no.8 (2024): 2301019, https://doi.org/10.1002/adom.202301019.

33. S. Mariotti, E. Kohnen, F. Scheler, et al., "Interface Engineering for High-Performance, Triple-Halide Perovskite–silicon Tandem Solar Cells," *Science* 381, no. 6653 (2023): 63–69, https://doi.org/10.1126/science.adf5872 2023-07.

34. A. Diercks, J. Petry, T. Feeney, et al., "Sequential Evaporation of Inverted FAPbI3 Perovskite Solar Cells – Impact of Substrate on Crystallization and Film Formation," *ACS Energy Letters* 10, no. 3 (2025): 1165–1173, https://doi.org/10.1021/acsenergylett.4c03315.

35. A. A. Said, E. Aydin, E. Ugur, et al., "Sublimed C60 for Efficient and Repeatable Perovskite-Based Solar Cells," *Nature Communications* 15, no. 1 (2024): 708, https://doi.org/10.1038/s41467-024-44974-0.

36. C. A. R. Perini, A. F. C. Mendez, T. Kodalle, et al., "Vapor-Deposited n = 2 Ruddlesden–Popper Interface Layers Aid Charge Carrier Extraction in Perovskite Solar Cells," *ACS Energy Letters* 8, no. 3 (2023): 1408, https://doi.org/10.1021/acsenergylett.2c02419

37. S. Hu, J. Pascual, W. Liu, et al., "A Universal Surface Treatment for p–i–n Perovskite Solar Cells," *ACS Applied Materials & Interfaces* 14, no. 50 (2022): 56290–56297, https://doi.org/10.1021/acsami.2c15989.

38. J. Li, P. Du, Q. Guo, et al., "Efficient All-Thermally Evaporated Perovskite Light-Emitting Diodes for Active-Matrix Displays," *Nature Photonics* 17, no. 5 (2023): 435–441, https://doi.org/10.1038/s41566-023-01177-1.

39. E. Siliavka, T. Pandelides, V. V. Shilovskikh, et al., "Additive Engineering of Sequentially Evaporated FAPbI3 Solar Cells," *Advanced Energy Materials* 15 (2025): 2500963, https://doi.org/10.1002/aenm.202500963.

Supporting Information

Additional supporting information can be found online in the Supporting Information section. **Supporting Note 1:** Device Fabrication. **Supporting Note 2:** Film and Device Characterization. **Supporting Note 3:** On the Choice of the Annealing Temperature and Duration. **Supporting Fig. 1:** A photograph of a statically deposited CsI layer on an M6 c-Si substrate with pseudo-square shape. **Supporting Fig. 2:** The five graphs in the top panel show the 1D XRD diffractograms for five different annealing temperatures for different annealing durations, all performed in N2-filled glovebox, measured on co-evaporated wide-bandgap perovskite films. In the bottom panel, the ratio of the perovskite phase (100) at ∼14.3° to that of PbI2 at ∼12.6°. The 160°C and 30 min condition was not selected, not only because of the very long annealing time but also based on other opto-electronic charcterisations performed, not presented here. **Supporting Fig. 3:** Left panel: Transmission and normalized PL spectrum overlay of perovskite film (without a top-FAI layer) processed on an MeO-2PACz covered ITO-glass substrate. Right panel: XRD diffractogram of an as-deposited film and after being annealed at 180°C for 5 min in the inert environment of a glovebox (O_2 and $H_2O < 0.1$ ppm). **Supporting Fig. 4:** 1D diffractograms from in-situ XRD azimuthally integrated from a 2D diffraction pattern at an incidence angle of 8 degrees. Results for samples with four different top-FAI thicknesses are presented: (A) Complete recorded diffractogram at room temperature before starting the annealing. (B) Complete recorded diffractogram at 180°C after 4:30 min of annealing. (C) 213 reflex of AB_2X_5 and 200 reflex of α-perovskite at room temperature before starting the annealing. (D) 213 reflex of AB_2X_5 and 200 reflex of α-perovskite at 180°C after 4:30 min of annealing. **Supporting Fig. 5:** Heatmap of in-situ XRD annealing experiments with 75 nm top-FAI. The vertical lines at 0 min and 7 min indicate the times when the diffractograms were extracted. Data from this experiment is grey colored in Figure 2, S3, and S5. On the left the calculated diffractogram of $C_sPb_2(Br_{0.4}I_{0.6})_5$ is shown. The calculations were done using VESTA [4]. **Supporting Fig. 6:** Relation of secondary phase in comparison with α-perovskite from in-situ XRD during annealing for (A) 002 AB_2X_5 reflex and 100 α-perovskite reflex and (B) 213 reflex of AB2X5 and 200 reflex of α-perovskite. In both graphs the same experiments are displayed as in Figure 2 and S3. **Supporting Fig. 7:** Evaporation rate, read by the QCM, as a function of time for all the four precursors. The plot including the QCM-read evaporation rate and thickness associated with FAI is that of the bottom-FAI with 125 nm thickness. Total time required for deposition of 125 nm and 305 nm of FAI and PbI2 (limiting the co-evaporated inorganic precursors thickness), respectively, was ≈17 and 63 min. **Supporting Fig. 8:** Top-view SEM images of the perovskite films fabricated with (A) 0, (B) 25, (C) 50, and (D) 75 nm top-FAI. The scale bar in the top left image is 1000 nm. **Supporting Fig. 9:** Cross-sectional SEM images of the perovskite films fabricated with (A) 0, (B) 25, (C) 50, and (D) 75 nm top-FAI. The scale bar in the top left image is 400 nm. **Supporting Fig. 10:** Normalized PL spectra of perovskite films with different top-FAI thicknesses (without any n-type contact layer) measured every 2 s over the total duration of 60 s. The green laser illumination intensity is about 0.5 Suns equivalent photon flux. **Supporting Fig. 11:** Time-evolved PLQY measured over 60 s under ≈0.5 Suns equivalent photon flux on the four sample types with different top-FAI thicknesses. **Supporting Fig. 12:** Average iVOC values measured after 6 and 60 s of continuous illumination with a 520 nm laser. The error bars are standard deviations calculated for at least 6 samples per fabrication process condition. **Supporting Fig. 13:** An example PV parameters obtained from light J–V measurements in a repeated, separately fabricated solar cell batch for top-FAI optimization other than that presented in the main text. **Supporting Fig. 14:** Maximum power point data of a solar cell processed using 25 nm top-FAI tracked over 10 min with power conversion efficiency of ∼16% stable over this time period. Measurement was performed in glovebox N2 atmosphere. **Supporting Fig. 15:** Comparing the PV parameters obtained from light J–V scans of the sequential evaporation approach presented in this work, where an FAI layer is deposited under the co-evaporated inorganic layer, with the commonly practiced method where the inorganic precursors are first co-evaporated into the substrate on which the organic halide salt, FAI, is deposited.

Three different top-FAI thicknesses were tested for the latter. Note that the co-evaporated inorganic layer of all the samples for the two approaches were processed in one deposition run so as to minimise the impact of additional factors contributing to the difference in the performance results across the different processing routes. **Supporting Fig. 16:** A photo, from the film side, of the sample holder accommodating 36 inch-by-inch substrates. **Supporting Fig. 17:** Maps of median values of (A) V_{OC}, (B) J_{SC}, and (C) PCE. The median value is calculated on 6 cells processed on each 1-inch by 1-inch substrate. **Supporting Fig. 18:** Cross-sectional SEM image of a tandem perovskite/silicon tandem solar cell (A) before and (B) after annealing at 180°C for 5 min. The scale bar at the bottom right of panel A is 200 nm. **Supporting Fig. 19:** (A) Light *J-V* curve of an example tandem cell with industrial textured bottom-cell. The top-cell perovskite absorber was processed using the three-step sequential evaporation method with 212.5 and 85 nm bottom- and top-FAI thicknesses (geometric factor of 1.7 was used to increase each separately deposited layer thickness). The insert table provides the PV parameters for the forward and reverse scans measurements. (B) EQE of the same device.